

RESEARCH ARTICLE

10.1002/2015JD023226

Key Points:

- Novel shipborne LF experiment to collect waveforms from deep ocean lightning
- Developed model to study the impact of return stroke parameters on ground wave
- Larger oceanic fields are unlikely due to changes in current rise, fall, or speed

Correspondence to:

F. G. Zoghzoghy,
fadiz@stanford.edu

Citation:

Zoghzoghy, F. G., M. B. Cohen, R. K. Said, N. G. Lehtinen, and U. S. Inan (2015), Ship-borne LF-VLF oceanic lightning observations and modeling, *J. Geophys. Res. Atmos.*, 120, 10,890–10,902, doi:10.1002/2015JD023226.

Received 5 FEB 2015

Accepted 14 SEP 2015

Accepted article online 18 SEP 2015

Published online 23 OCT 2015

Ship-borne LF-VLF oceanic lightning observations and modeling

F. G. Zoghzoghy¹, M. B. Cohen², R. K. Said³, N. G. Lehtinen¹, and U. S. Inan^{1,4}

¹Department of Electrical Engineering, Stanford University, Stanford, California, USA, ²School of Electrical and Computer Engineering, Georgia Institute of Technology, Atlanta, Georgia, USA, ³Vaisala, Inc., Louisville, Colorado, USA, ⁴Electrical Engineering Department, Koç University, Sariyer, Turkey

Abstract Approximately 90% of natural lightning occurs over land, but recent observations, using Global Lightning Detection (GLD360) geolocation peak current estimates and satellite optical data, suggested that cloud-to-ground flashes are on average stronger over the ocean. We present initial statistics from a novel experiment using a Low Frequency (LF) magnetic field receiver system installed aboard the National Oceanic Atmospheric Agency (NOAA) Ronald W. Brown research vessel that allowed the detection of impulsive radio emissions from deep-oceanic discharges at short distances. Thousands of LF waveforms were recorded, facilitating the comparison of oceanic waveforms to their land counterparts. A computationally efficient electromagnetic radiation model that accounts for propagation over lossy and curved ground is constructed and compared with previously published models. We include the effects of Earth curvature on LF ground wave propagation and quantify the effects of channel-base current risetime, channel-base current falltime, and return stroke speed on the radiated LF waveforms observed at a given distance. We compare simulation results to data and conclude that previously reported larger GLD360 peak current estimates over the ocean are unlikely to fully result from differences in channel-base current risetime, falltime, or return stroke speed between ocean and land flashes.

1. Introduction

Lightning flashes are both powerful and frequent with more than a billion discharges occurring around the globe every year [Christian *et al.*, 2003]. Although 90% of the lightning activity occurs over land, various studies using optical satellite observations [Turman, 1977] and electromagnetic radiation data from lightning geolocation systems, which estimate the peak current magnitude for each lightning discharge, suggested that cloud-to-ground (CG) flashes are stronger over the ocean than over land [Lyons *et al.*, 1998; Orville and Huffines, 2001; Fullekrug *et al.*, 2002; Cummins *et al.*, 2005; Orville *et al.*, 2011; Said *et al.*, 2013; Hutchins *et al.*, 2013]. The network-reported peak current estimates are (generally) inferred by looking at the average strength of the lightning radiation detected at multiple sensors, after accounting for propagation [Cummins *et al.*, 1998]. The factors that contribute to the observed oceanic enhancement in network-reported peak currents and the sources that govern the magnitude of the return stroke peak currents are still poorly understood and are of interest to those concerned with the safety of aircrafts, vessels, ground-based electronic systems, and are essential to the understanding of thunderstorm electrification and behavior [MacGorman and Morgenstern, 1998; Williams *et al.*, 2005].

The majority of lightning flashes are either classified as CG or as intracloud (IC) discharges, with either a positive or a negative polarity. CGs are more dangerous to ground assets and account for (approximately) 25% of the total lightning activity [Rakov and Uman, 2007, pp. 4]. Roughly 90% of CGs are negative (–CG) and consist of multiple return strokes, separated by tens to hundreds of milliseconds. The initial stroke follows a stepped leader, while subsequent ones can recur either along the same channel following a dart leader or in a nearby channel following a dart-stepped leader [Rakov and Uman, 2007, pp.164–165]. Peak currents of the individual strokes do not correlate well with the impulse charge moment (computed using the first 2 ms) in a CG flash [Cummer *et al.*, 2013]. The bulk of the total charge is transferred to ground by long-lasting (and weaker) continuing currents, which last hundreds of milliseconds [Rakov and Uman, 2007, pp. 222]. Nevertheless, peak current measurements quantify the intensity of the impulsive phase of the return stroke and are of great practical interest.

Lightning strokes radiate across a wide spectrum of electromagnetic waves with a peak in the Very Low Frequency (VLF; 3–30 kHz) band, where waves propagate efficiently in the Earth-ionosphere waveguide (few dB attenuation per 1000 km). The electromagnetic pulse (EMP) associated with the return stroke is known as a radio atmospheric, or sferic for short, and can be used to geolocate lightning strokes and as a surrogate measure to study the underlying lightning physics. In our study we use data from the Global Lightning Detection (GLD360) network to identify lightning strokes that occur around our experimental setup. GLD360, operated by Vaisala Inc., consists of VLF sensors that monitor lightning activity globally [Said *et al.*, 2010]. GLD360 has a 57% flash detection rate and estimates peak currents for the individual strokes with 21% (6% mean (geometric mean) magnitude error, though the source type (IC versus CG) is not currently reported [Said *et al.*, 2010, 2013]. The validation was done by comparing GLD360 peak current estimates with those reported by the National Lightning Detection Network (NLDN), the accuracy of which has in turn been evaluated using triggered flashes at Camp Blanding (but is limited to continental U.S. coverage) [Cummins and Murphy, 2009; Nag *et al.*, 2011; Mallick *et al.*, 2014a]. Mallick *et al.* [2014b] compared GLD360 peak currents to ones measured in triggered lightning and reported a 67% flash detection rate and a 27% median absolute current estimation error for GLD360.

Cooray [1987]; Cooray *et al.* [2000] showed that simple mathematical models, using equations from Norton [1936], could be used to account for the ground wave propagation of the electromagnetic radiation fields over a flat Earth, and validated the analytical model against collected lightning waveforms. Due to the planar assumptions, the model from Cooray [1987] did not account for Earth curvature and was not valid for propagation distances greater than 500 km. Marshall [2012] presented a finite difference time domain (FDTD) model of the lightning sferic which solved for the fields in a spherical coordinate system, inherently accounting for Earth curvature and ground conductivity. In section 3, we present a ground wave model built around a frequency domain numerical technique, which accounts for the physics of propagation and compare simulation results with the analytical model from Cooray [1987] and to the FDTD technique detailed in Marshall [2012].

Said *et al.* [2013] used GLD360 data to show that peak currents for ocean –CG flashes are 22%–88% higher compared to land –CGs within small coastal regions. Other studies using various geolocation systems supported these observations showing stronger lightning over the ocean, with sharp enhancements along the coastlines [Cummins *et al.*, 2005; Orville *et al.*, 2011]. Lyons *et al.* [1998] used National Lightning Detection Network (NLDN) data, which consists of VLF/Low Frequency (LF; 30–300 kHz) sensors, over the continental U.S. to show that the median NLDN-reported peak currents for initial –CG strokes are higher over saltwater than over land [Orville and Huffines, 2001]. Orville and Huffines [2001] aggregated 10 years of NLDN data that suggest that peak current magnitudes increase from 27 kA to over 30 kA along the eastern U.S. coast and the Gulf coast. Interestingly, most of these studies found that the ocean enhancement is less pronounced for subsequent –CGs and for positive CG (+CG) flashes, which do not show sharp coastline transitions for median peak currents [Cummins *et al.*, 2005; Orville *et al.*, 2011; Said *et al.*, 2013]. The World Wide Lightning Location Network (WWLLN) also reports stronger strokes over the ocean with sharp transitions along much of the coastlines [Hutchins *et al.*, 2013].

Many (sometimes contradicting) explanations for the larger EMPs over the oceans were presented. Lyons *et al.* [1998] attributed the enhancement to the high conductivity of saltwater but did not offer an explanation for the higher peak current inland along the U.S./Mexican borders. The higher radiated fields could result from more intense flashes in oceanic thunderstorms due to meteorological or climatological differences over the ocean. For instance, Cooray *et al.* [2014] suggested that the enhancement is due to differences in the charge structure in ocean clouds as the unfavorable conditions for the formation of the lower positive charge layer lead to lightning initiation at higher cloud potentials (compared to their land counterparts), resulting in larger peak currents in initial –CGs. The authors argued that the positive charge pocket did not promote +CG strokes, which is consistent with the lack of enhancement in +CGs. Chronis [2012] also showed a dependence of CG peak currents on seawater salinity, a trend that is absent for +CGs. Zoghzoghy *et al.* [2013] quantified the occurrence probability of a lightning discharge as a function of distance and time following an initial discharge as a proxy method for monitoring the charging processes in the cloud using GLD360 data and showed that the recoveries following oceanic CGs are different than those following land CGs, hinting to meteorological differences between oceanic and land thunderstorms. Cummins *et al.* [2005] argued that the primary effects are in the attachment process to saltwater in initial –CGs, following a stepped leader, which agrees with the lack of peak current enhancement in –CGs that strike freshwater over the Great Lakes area in the U.S. [Cooray *et al.*, 2014; Said *et al.*, 2013]. Cooray and Rakov [2011] studied the effect of ground conductivity on electromagnetic

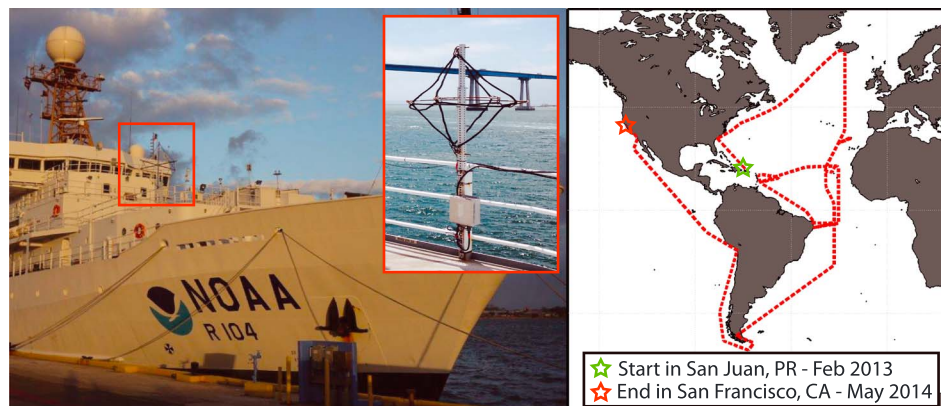


Figure 1. Picture of the Ronald W. Brown research vessel and the LF receiver magnetic loop antenna. (right) Map of the voyage starting from San Juan, Puerto Rico, in February 2013 and ending in San Francisco, California, U.S., in May 2014.

propagation and concluded that the more efficient propagation over the highly conductive saltwater (than over land) is unlikely to explain higher peak-radiated observations over the ocean. In addition, the geographical distribution of the network sensors could lead to systematic biases in peak current estimation due to the nonuniform coverage of deep oceanic areas and to sensor thresholds, which could skew the distribution of detected peak currents toward more powerful (higher peak current) events [Said *et al.*, 2013]. In addition, Tyahla and Lopez [1994] investigated peak current distributions in two coastal regions in Florida and did not notice more intense field changes from sea lightning, indicating that the transition may be more gradual in some regions like Florida, consistent with Orville and Huffines [2001]; Cooray *et al.* [2014]. Also, radiation fields could be enhanced without increasing the magnitude of the lightning currents inside the channel, by a change in the return stroke velocity or the channel-base current risetime, resulting from physical differences in the attachment process and leading to changes in the lightning radiation patterns.

In this paper, we investigate the impact of return stroke parameters on the lightning waveform and the extent to which they could potentially contribute to the GLD360-reported peak current enhancement, using a ground wave lightning radio remote sensing model and new LF data collected in the vicinity of oceanic storms. In section 2, we present our lightning experiment in which we deploy an LF receiver system with 1 MHz sampling frequency aboard the NOAA Ronald W. Brown research vessel. When reasonably close (within several hundred kilometers) to oceanic thunderstorms, the LF receiver detects the impulsive radio emissions from the lightning source. In section 3, we present a physical model that we use to simulate the ground wave portion of the lightning waveform, resulting from an arbitrary current profile along the lightning channel. We quantify the effect of Earth curvature and ground conductivity on LF-VLF propagation, and conduct a sensitivity analysis to study different return stroke parameters that could contribute to the observed enhancement in peak current estimates of oceanic lightning. In section 4, we process and analyze thousands of collected waveforms and compare them to model-simulated ground waves.

2. Observations

We conducted a shipborne LF experiment to investigate the physics of oceanic CG lightning and the observed enhancement in GLD360-reported peak currents over the ocean. We deployed a highly sensitive Atmospheric Weather Electromagnetic System for Observation Modeling and Education (AWESOME) instrument aboard the Ronald W. Brown NOAA research vessel, as shown in Figure 1, to collect nearby lightning waveforms, geolocated using the global GLD360 network. Our broadband LF instrument was similar to the AWESOME VLF receiver described by Cohen *et al.* [2010] but sampled the signal at a higher rate of 1 MHz, after the signal passes through an analog anti-aliasing filter with a cut-off frequency ≈ 500 kHz. The receiver consisted of three wire-loop antennas (57 cm \times 57 cm), orthogonal to each other, and each sensitive to the component of the magnetic field orthogonal to the plane of the loop. Since the vertical magnetic fields are typically much smaller near the ground, the horizontal loop is not required in many applications but was useful in our experiment to account for the sway of the ship.

Table 1. Attenuation Function $A(z)$ With Altitude for MTLL and MTLE

Model	$A(z)$
MTLL	$1 - z/L$
MTLE	$e^{-z/\lambda}$

We collected LF data from strokes located using GLD360, a long-range geolocation network that has been in operation since 2009. GLD360 uses a global network of VLF sensors that use magnetic direction finding and time-of-arrival methodologies to achieve a median accuracy of 2.5 km, a CG flash detection efficiency of 57% and estimates return stroke peak currents with a mean magnitude error of 21% [Said *et al.*, 2010, 2013] and a median absolute current estimation error of 27% [Mallick *et al.*, 2014b]. Our experiment started in February 2013 in San Juan, Puerto Rico, and ended in May 2014 in San Francisco, California, U.S.A., as shown in the map of the voyage in Figure 1. Throughout the experiment, the system locally stored broadband LF data for tens of thousands of GLD-reported return strokes within a 750 km radius from the ship. One second of LF data was transmitted daily back to Stanford University to help monitor data quality.

We are interested in the ground wave portion of the lightning sferic, which, unlike the sky waves, propagates directly from the source lightning to the receiver without reflecting off of the ionosphere. The ground wave contains the direct signature of the nearby stroke (after 1000 km the sky waves dominate the sferic) and could potentially be used to infer properties of the current profile inside the source lightning channel without modeling ionospheric interactions that vary with frequency and time of day, and require further assumptions (such as the ionospheric profile with altitude). Thus, when reasonably close, our LF receiver captures radio emissions from the lightning source and provides a higher resolution waveform than the one captured using VLF components traveling in the Earth-ionosphere waveguide (in terms of frequency, time, and direct lightning-to-receiver propagation). Next, we present a ground wave model, which we use to investigate the physics of the ground wave and to complement our data with theory.

3. Ground Wave Modeling

3.1. Analytical Model

We use return stroke models to specify the current profile $i(t, z)$ as a function of time t and altitude z along the lightning channel, which we couple with a propagation model to simulate lightning waveforms. Generally, return stroke models fall under one of four categories: gas dynamic models, electromagnetic models, distributed-circuit models, and engineering models [Rakov and Uman, 2007, pp. 394]. Rakov and Uman, 2007 [2007, pp. 395–410] presents detailed descriptions and analyses of these various models. Engineering models relate the temporal current profile at altitude z to the current profile at the base of the lightning channel ($z = 0$, t) as shown in equation (1), where $u(t)$ is the unit step function, $A(z)$ is the attenuation of the amplitude of the current with altitude, and v_{rs} is the return stroke speed.

$$i(z, t) = u(t - z/v_{rs}) A(z) i(z = 0, t - z/v_{rs}) \quad (1)$$

We focus on engineering models, which have a small number of adjustable parameters (3–5 parameters), such as peak current, return stroke speed, and channel current risetime, which are enough to specify the spatial and temporal channel current profile $i(z, t)$. The shape of the channel base current $i(z = 0, t)$ is restricted to a family of curves with linear rise and exponential fall, which are specified using three parameters, a peak current value I_{peak} at time t_{rise} , and exponential falltime constant τ_{fall} , as shown in equation (2).

$$i(z = 0, t) = \begin{cases} 0 & , t < 0 \\ (I_{\text{peak}}/t_{\text{rise}}) t & , 0 \leq t \leq t_{\text{rise}} \\ I_{\text{peak}} e^{-\left(\frac{t-t_{\text{rise}}}{\tau_{\text{fall}}}\right)^2} & , t > t_{\text{rise}} \end{cases} \quad (2)$$

We use the modified transmission line model with linear current decay with height (MTLL) [Rakov and Dulzon, 1987] and the modified transmission line model with exponential decay with height (MTLE) [Nucci *et al.*, 1988], which only differ in the way they model the current attenuation with altitude, $A(z)$. The two attenuation functions are shown in Table 1, where L is the MTLL length of the lightning channel and λ is the MTLE exponential decay constant with altitude.

Simple analytical models can be used to propagate the radiations fields resulting from lightning in a planar configuration (flat Earth) with finite ground conductivity. The radiation field $dB(j\omega)$ resulting from a channel segment dz , at an elevation z , propagating to a distance d over a perfect conductor is given by equation (3), where $c = 2.998 \times 10^8 \text{ m s}^{-1}$ is the speed of light in free space, $\mu_0 = 4\pi \times 10^{-7} \text{ H m}^{-1}$ is the magnetic permeability of free space, μ_r is the relative permeability, $\epsilon_0 = 8.854 \times 10^{-12} \text{ C m}^{-1}$ is the permittivity of free space, ϵ_r is the relative permittivity, ω is the angular frequency, $j^2 = -1$, and $I(j\omega, z)$ is the Fourier transform of $i(t, z)$ given by equation (4).

$$dB(j\omega) = \frac{j\omega\mu_0\mu_r}{2\pi c\sqrt{d^2+z^2}} I(j\omega, z) \exp(j\omega t - j\omega \frac{\sqrt{d^2+z^2}}{c}) dz \quad (3)$$

$$I(j\omega, z) = \int_{-\infty}^{+\infty} i(t, z) \exp(-j\omega t) dt \quad (4)$$

The frequency domain radiation field $B(j\omega)$ is computed by integrating over all the radiation elements along the length of the channel L after accounting for attenuation due to finite ground conductivity σ , as shown in equation (5), where $G(j\omega, z, d, \sigma)$ is the attenuation function derived by Norton [1936] given by equation (6). The time domain radiation fields $B(t)$ are computed using the inverse Fourier transformation given by equation (7) and expressions for the components of $G(j\omega, z, d, \sigma)$ are given by equations (8)–(10), where erfc stands for the complementary error function and $\{\epsilon_0\}$ is the (unitless) numerical value of the permittivity of free space.

$$B(j\omega) = \int_{z=0}^L G(j\omega, z, d, \sigma) dB(j\omega) \quad (5)$$

$$G(j\omega, z, d, \sigma) = 1 + j\sqrt{\pi\alpha} \exp(-\alpha) \text{erfc}(-j\sqrt{\alpha}) \quad (6)$$

$$B(t) = \int_{-\infty}^{+\infty} B(j\omega) \exp(j\omega t) d\omega \quad (7)$$

$$\alpha = \frac{2j\omega\sqrt{d^2+z^2}\beta^2}{c(1-\gamma)^2} \quad (8)$$

$$\beta^2 = \frac{j\omega}{j\omega\epsilon_r\{\epsilon_0\} - \mu_r\mu_0\sigma c^2} \quad (9)$$

$$\gamma = \frac{z/d - \beta}{z/d + \beta} \quad (10)$$

3.2. Ground Wave Full-Wave Method

We built a physical model that simulates the ground wave portion of the lightning sferic for a set of return stroke parameters and propagation properties. The model is useful to visualize the impact of source parameters (such as a faster return stroke speed or a shorter current risetime) on the shape of the ground wave while accounting for ground propagation.

We use return stroke engineering models to specify the spatial and temporal current profile $i(t, z)$ inside the lightning channel. We use the full-wave method (FWM) detailed in Lehtinen and Inan [2008, 2009] and Lehtinen *et al.* [2012] to radiate and propagate the fields and to compute the ground wave portion of the lightning sferic ground wave full-wave method (gwFWM), while accounting for Earth curvature and for finite ground conductivity. We find the fields in a stratified medium created by an arbitrary combination of harmonically varying sources, with arbitrary electromagnetic properties of the medium (i.e., permittivity tensor). We apply Snell's law in the plane-stratified medium to calculate the fields for each horizontal wave vector component k_{\perp} in the Fourier space over horizontal coordinates d_{\perp} . The technique recursively computes the

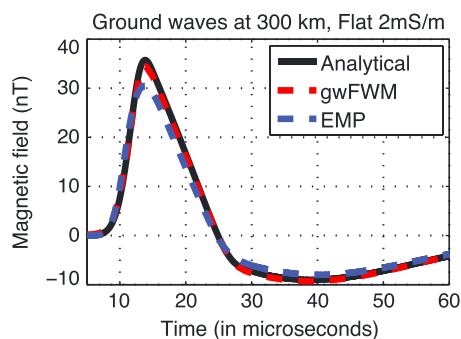


Figure 2. Simulated ground waves using the gwFWM (in solid red), the analytical approximations (in solid black), and the FDTD EMP (in dashed blue) for the same input parameters: MTL model, 2 μs risetime, 30 μs falltime, 100 kA peak current, 3 km source height, $\frac{2c}{3}$ return stroke speed, flat 2 mS m^{-1} Earth, and frequency content up to 500 kHz.

reflection coefficients and mode amplitudes and is stable against numerical “swamping,” which is inherent in other techniques [Budden, 1985, pp. 574–576]. Lehtinen *et al.* [2012] described a general curvilinear stratified system to include the effects of curvature into the planar method by considering a general curvilinear stratified system with anisotropic media and validated the results for an isotropic medium in a cylindrically stratified system. The FWM model was validated in many VLF ionospheric applications [Lehtinen and Inan, 2008, 2009; Cohen *et al.*, 2011, 2012; Graf *et al.*, 2013]. The finite element, frequency domain method calculates the frequency response $H(j\omega, z, d, \sigma, R_{\text{curv}})$ which includes the radiation fields and the attenuation/dispersion due to finite conductivity σ and curvature R_{curv} . We only need to compute $H(j\omega, z, d, \sigma, R_{\text{curv}})$ once, then we can construct, in parallel, multiple ground waves with different lightning source parameters (but same propagation properties d , σ , and R_{curv}) following a frequency domain construction similar to the one shown for the analytical model in section 3.1.

3.3. Model Comparison

Figure 2 shows three ground waves simulated at 300 km, the first (in dashed red) using the gwFWM, the second (in solid black) using the analytical model, and the third (in dashed blue) using the FDTD EMP from Marshall [2012], computed using the same input parameters: (i) MTL return stroke model with 2 μs current risetime, 30 μs falltime, 100 kA peak current, 3 km source height, and $\frac{2c}{3}$ return stroke speed; (ii) wave propagation over flat Earth, with finite ground conductivity of 2 mS m^{-1} , and (iii) frequency content up to 500 kHz. The shape of the gwFWM ground wave is similar to the waveforms of other two models. The peak of the gwFWM ground wave is within 5% and 15% from the peaks of the analytical and FDTD waveforms, respectively. The 15% difference between gwFWM and FDTD EMP could be due to numerical dispersion or other approximations that are slightly different in time domain and frequency domain methods. We repeat the comparison for different current profiles $i(t, z)$ and find similar results that validate our gwFWM model. We limit the comparison among the three models to a flat Earth due to the planar limitations of the analytical model.

The three models account for a finite ground conductivity, though only gwFWM and FDTD EMP account for curvature. The waveforms from gwFWM and FDTD EMP are consistent, but each model offers different advantages. FDTD EMP (time domain) could be used to simulate nonuniform horizontal conductivity profiles (varying ground conductivity $\sigma(d)$ as a function of distance d) but is computationally expensive, taking several hours to evaluate each run. Thus, FDTD EMP could model the ocean-land boundary and is useful to investigate the electromagnetic reflections off of the ocean-land transition and to compare the efficiency of electromagnetic source excitation over the ocean and over land (due to the stronger image current over higher conductivity ground). We note that we only address the efficiency of electromagnetic excitation due to differences in the amplitude of image currents and do not address or capture differences in the attachment process or in the current wave-front behavior between ocean and land CGs. We use the FDTD EMP to simulate the same lightning stroke twice, once over the ocean with 300 km of ocean propagation ($\sigma(d) = 5 \text{ S m}^{-1}$ for all d) and a second time over land with only 0.25 km of land propagation and the remaining 299.75 km of propagation over the ocean ($\sigma(d) = 2 \text{ mS m}^{-1}$ for $d \leq 0.25 \text{ km}$ and $\sigma(d) = 5 \text{ S m}^{-1}$ for $d > 0.25 \text{ km}$). We compare the simulated ground waves and find them to be visually identical, suggesting that electromagnetic source excitation over land and ocean does not contribute to the observed electromagnetic enhancement. We also probe the fields in the second run at the ocean-land boundary and do not find any reflections from the abrupt transition in ground conductivity at $d = 0.25 \text{ km}$. The results suggest that the sharp GLD360-reported enhancement along the coastlines is not due to stronger image currents over the ocean or to electromagnetic reflections, consistent with the multisection mixed paths lightning radiation modeling presented by Cooray and Cummins [2009]. The sharp transition is thus either due to physical differences at the source lightning and/or due to (artificial) systematic biases in network-estimated peak currents over the ocean which could result from network inaccuracies such as range filtering. Typically, electromagnetic geolocation

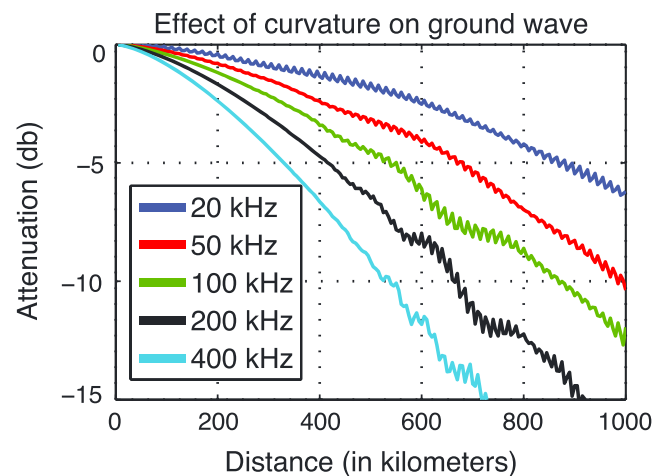


Figure 3. Attenuation due to Earth curvature (shown on a dB scale) as a function of propagation distance (in kilometers) for different frequency components: 20 kHz (in blue), 50 kHz (in red), 100 kHz (in green), 200 kHz (in black), and 400 kHz (in cyan).

networks, such as NLDN and GLD360, suffer from range filtering, due to the fact that weak events far from sensors are likely to be missed. This artifact biases the distribution of peak currents and leads to overestimates of the corresponding mean, median, or geometric mean.

The gwFWM (frequency domain) model is limited to uniform horizontal conductivity profiles but is computational fast, taking 5 to 20 s to evaluate each run. This efficiency offers many practical advantages and enables us to conduct sensitivity analyses (section 3.5). We use the gwFWM to study the impact of Earth curvature on ground wave propagation (section 3.4), the effects of different lightning parameters on the simulated waveform (section 3.5), and to compare our LF data to the simulated waveforms (section 4).

3.4. Earth Curvature

We use gwFWM to study the impact of Earth curvature on VLF and LF ground wave propagation. Figure 3 shows the attenuation due to Earth curvature ($R_{\text{Earth}} = 6371$ km) as a function of propagation distance, parameterized by frequency (only depends on Earth curvature and does not depend on conductivity). We generate the attenuation for each distance, frequency pair (d_i, f_j) by computing the ratio of the magnitude response of frequency f_j at distance d_i for a curved Earth to the one of a flat Earth, and plot them on a dB scale. Ground curvature acts as a low-pass filter with increasing attenuation for larger frequency components and for longer propagation paths. The attenuation of the 20 kHz component (in blue) goes from <1 dB at 200 km to ~ 6 dB at 1000 km. Higher frequency components such as 200 kHz (in black) and 400 kHz (in cyan) attenuate faster, reaching 6 dB attenuation at 400 km and 500 km, respectively. We note that these results are specific to the ground wave portion of the spheric (they do not account for ionospheric reflections) and are important when comparing theoretical ground waves to data, as the attenuation due to curvature varies for different frequency components. We note that the oscillations in the results of Figure 3 are due to model approximations in the k space to d space conversion. The attenuation curves could also be used to find an empirical attenuation formula $C(j\omega, d)$ that could be added to the analytical model to account for the impact of curvature, by adding $C(j\omega, d)$ to equation (5).

In the next section, we conduct a one factor at a time sensitivity analysis where we hold all gwFWM inputs constant and vary one at a time to study its impact on the simulated waveform.

3.5. Sensitivity Analysis

We specify the current profile $i(t, z)$ using engineering return stroke models. The peak current parameter I_{peak} , corresponding to the peak value of the channel-base current $i(t, z = 0)$, tunes the magnitude of $i(t, z)$, and results in a (linear) scaling of the output waveform. If all else is constant, two simulations s_1 and s_2 with $I_{s_1}^{\text{peak}} = a I_{s_2}^{\text{peak}}$ will result in $i_{s_1}(t, z) = a i_{s_2}(t, z)$ and $B_{s_1}(t) = a B_{s_2}(t)$. The two output waveforms are similar in shape but scaled in magnitude. Next, we explore the (nonlinear) effects of current risetime, current falltime, and return stroke speed on the simulated waveform.

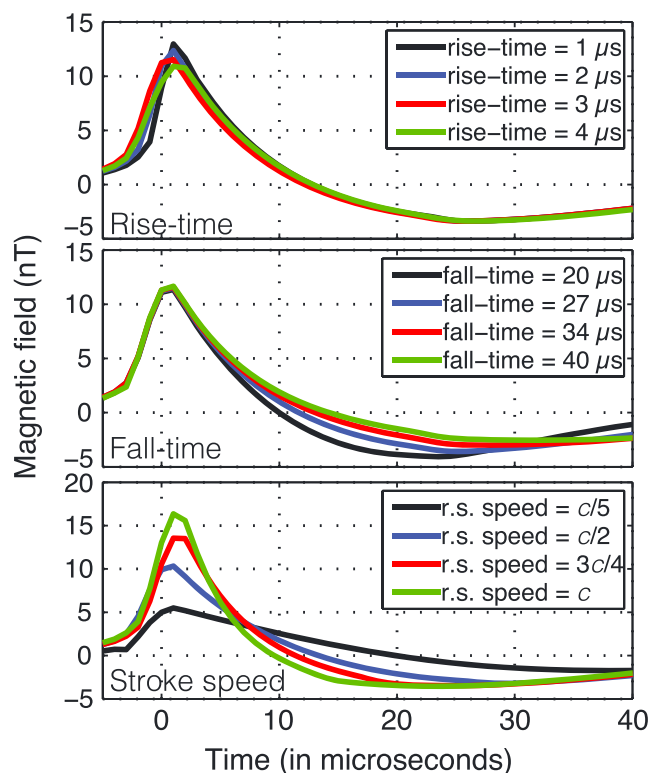


Figure 4. One factor at a time (OFAT) sensitivity analyses of (top) the channel-base current risetime, (middle) the current falltime, and (bottom) the return stroke speed on simulated waveforms at 500 km. (top) Simulated waveforms with current risetimes of 1 μs (in black), 2 μs (in blue), 3 μs (in red), and 4 μs (in green). (middle) Simulated waveforms with current falltimes of 20 μs (in black), 27 μs (in blue), 34 μs (in red), and 40 μs (in green). (bottom) Simulated waveforms with return stroke speeds of $c/5$ (in black), $c/2$ (in blue), $3c/4$ (in red), and c (in green).

Figure 4 consists of three panels corresponding to three sensitivity analyses useful to study the impact of current risetime, current falltime, and return stroke speed on the simulated waveform, respectively. Figure 4 (top) shows four simulated ground waves at 500 km from four gwFWM runs with the current risetime on the ground varying between 1 μs (in black) and 4 μs (in green). The other model parameters are held constant (MTLE, $\beta_{\text{decay}} = 1.08$ km, 30 μs falltime, $\frac{c}{2}$ return stroke speed, 100 kA peak current, $R_{\text{Earth}} = 6371$ km, $\sigma = 5$ S m⁻¹). We analyze the peak value, the 20%–90% risetime, and the 90%–20% falltime of the ground waveform (using the extraction tool introduced in section 4.1). The simulated ground waves have 20%–90% risetime and peak values of 1.43 μs and 26.66 nT (1 μs current risetime; in black), 1.77 μs and 25.14 nT (2 μs current risetime; in blue), 2.29 μs and 23.63 nT (3 μs current risetime; in red), 2.88 μs and 22.29 nT (4 μs current risetime; in green). We measure a ~17% drop in the LF waveform peak and a ~100% increase in the 20%–90% risetime as we vary the current risetime from 1 μs to 4 μs. These results suggest that different channel-base current risetimes affect the shape of the corresponding waveform and that a change in current risetime at the lightning source could be inferred by analyzing the 20%–90% risetime, which should be observable in our LF data and could potentially provide more insight into the underlying attachment and return stroke processes. In section 4.2 we use this approach and apply it to collected waveforms to estimate the difference in current risetime between oceanic and land CGs.

NLDN and various other LF geolocation networks use the LF peak of the ground wave to estimate peak currents [Cummins et al., 1998; Nag et al., 2014] and calibrate their algorithms using subsequent return strokes from triggered lightning experiments [Nag et al., 2011; Mallick et al., 2014a]. We note that the ~17% change in the waveform peak from shorter risetimes could potentially lead to errors in the estimation of peak currents for initial negative and positive CGs, which tend to have current risetimes much different (5 times longer) than current risetimes of subsequent negative strokes [Berger et al., 1975].

We conduct a similar analysis in Figure 4 (middle) where we vary the channel base current falltime from 20 μs (in black) to 40 μs (in green) while holding other parameters constant (MTLE, $\beta_{\text{decay}} = 1.08$ km, 3 μs risetime, $\frac{c}{2}$

return stroke speed, 100 kA peak current, $R_{\text{Earth}} = 6371 \text{ km}$, $\sigma = 5 \text{ S m}^{-1}$), and plot the simulated ground waves at 500 km. The results suggest that current faltime has no effect on the rise and on the peak of the ground wave, and mostly leads to a change in the shape of the tail of the waveform; longer current falltimes produce longer waveform falltimes. Thus, a change in the faltime of the channel base current (due to a difference in the attachment process or the ground conductivity) is unlikely to explain the observed GLD360 oceanic enhancement.

In Figure 4 (bottom), we hold all parameters constant (MTLE, $\beta_{\text{decay}} = 1.08 \text{ km}$, $3 \mu\text{s}$ risetime, $30 \mu\text{s}$ falltime, 100 kA peak current, $R_{\text{Earth}} = 6371 \text{ km}$, $\sigma = 5 \text{ S m}^{-1}$) and vary the return stroke speed along the lightning channel between $c/5$ (in black) and c (in green), and plot the simulated waveforms at 500 km. Our results show that a change in the return stroke speed leads to a change in both the shape and in the peak of the ground wave, consistent with previous results [Thottappillil and Uman, 1993]. The simulation waveforms show that faster return strokes lead to narrower pulses with larger peaks. The theoretical model shows that a change in the lightning return stroke speed is measurable in the waveform and should be captured by our LF data. Thus, in case the oceanic enhancement is due to faster return stroke speeds (due to a difference in the attachment process or the ground conductivity), we would observe different shapes for oceanic and land LF ground waves (narrower for ocean CGs), a possibility that we discuss in section 4.3.

4. Data Analysis

4.1. Statistical Tools

We introduce two statistical tools that we use to analyze the collected LF waveforms and to compare them to simulation waveforms. Throughout the analysis, we only study initial $-$ CGs, which show a sharp transition in peak currents along the coastlines, a trend that is absent for $+$ CGs and for subsequent strokes $-$ CGs. The first tool is an automated feature extraction technique that goes through all the collected LF time series, uses cubic spline interpolation (other interpolation technique could be used) to upsample the data to 30 MHz (to provide $\sim 33.3 \mu\text{s}$ resolution of the extracted features), and extracts features such as 20%–90% risetime, 20%–90% linear rise slope, waveform peak, 90%–20% falltime, 90%–20% slope, and peak to zero crossing time. We apply the feature extraction technique to an oceanic $-$ CG, 284.5 km from the ship, on 17 July 2013 at 08:15:05 UTC and display the waveform in Figure 5. This technique enables us to study features in the individual sferics and to develop a better understanding of the impact of various physical lightning properties on the ground wave features. The second tool is a waveform aggregation technique which is useful to capture average effects and to compare the average ground waves of different groups of lightning events (as later discussed in section 4.2). The technique goes through the lightning sferics, aligns them in time, computes their average waveform, and compares it to the average sferic of other groups. In sections 4.2 and 4.3, we use both techniques to analyze thousands of waveforms and to study the impact of ground conductivity, return stroke speed, and peak currents on the observed LF waveforms.

4.2. Ground Conductivity and Current Risetime

We apply the feature extraction tool to 17,974 initial $-$ CGs and use the (20%–90% risetime, lightning-to-receiver distance) pairs to generate Figure 6. We divide the initial strokes into three categories, the first (in blue) consists of ocean $-$ CGs that propagate over the ocean ($>90\%$ of the propagation path is over the ocean), the second (in green) consists of land $-$ CGs that propagate over land ($>90\%$ of the propagation path is over land; this occurs when the ship is docked), and the third (in cyan) consists of 683 land $-$ CGs that propagate to the ship over a mixed path, $>50\%$ of which consists of ocean propagation (occurs when the ship is sailing close to land). For each category, we group the events in 25 km distance bins and compute their median 20%–90% risetime. We plot the results and include the 25th and 75th percentile error bars.

Figure 6 shows that ground waves from ocean strokes with ocean propagation (first category; in blue) have lower risetimes than waveforms from land strokes with land propagation (second category; in green). The median risetimes of the first category (in blue) are consistently lower than the 25th percentile of the second category (in green). The third category (in cyan), which consists of land strokes with mixed land-ocean paths, has 20%–90% risetimes that fall between the other two categories, with risetimes closer to ocean strokes with ocean propagation, and much lower than those of land strokes with land propagation. This shows that ground waves from land strokes have significantly lower risetimes when they partially propagate over the ocean (in cyan) than when they only propagate over land (in blue). Our results suggest that poor ground conductivities attenuate the higher-frequency components, smoothing the rising slope of the waveform. We

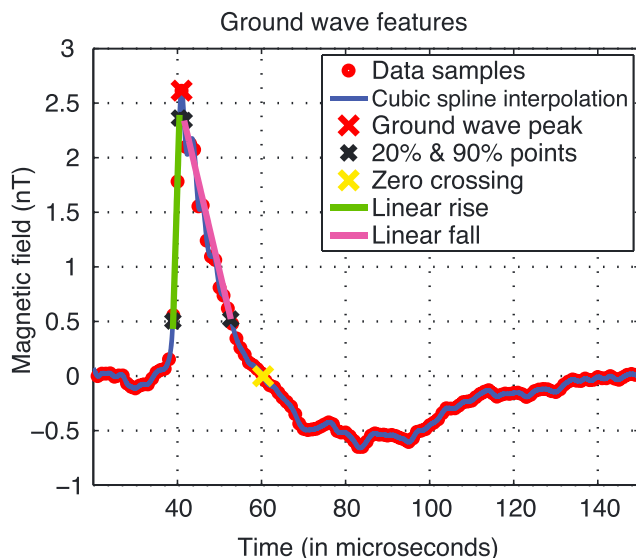


Figure 5. Feature extraction tool applied to a waveform corresponding to a GLD360-reported stroke that occurred on 17 July 2013 08:15:05 UT at (lat=33.49, lon=-76.99), with -19 kA reported peak current, 285 km from the location of the ship.

further investigate this trend using the gwFWM model and simulate two ground waves at 400 km for the same lightning stroke (MTLE, $\beta_{decay} = 1.08$ km, $1 \mu\text{s}$ risetime, $30 \mu\text{s}$ falltime, $\frac{c}{3}$ return stroke speed, 100 kA peak current, $R_{Earth} = 6371$ km), one propagation over ocean propagation ($\sigma_{ocean} = 5 \text{ S m}^{-1}$) and the other over land ($\sigma_{land} = 2 \text{ mS m}^{-1}$). We measure $1.65 \mu\text{s}$ and $3.64 \mu\text{s}$ risetimes at 400 km for ocean and land propagation, respectively, matching closely with our LF data.

Our experimental and theoretical observations suggest that lower ground conductivity attenuates the LF components and leads to a measurable change in the ground wave 20%–90% risetime. Our results are in agreement with previous studies that investigate the impact of ground conductivity on LF radiation fields [Bardo et al., 2004; Cummins et al., 2005]; Lower ground conductivities attenuate the highest frequency

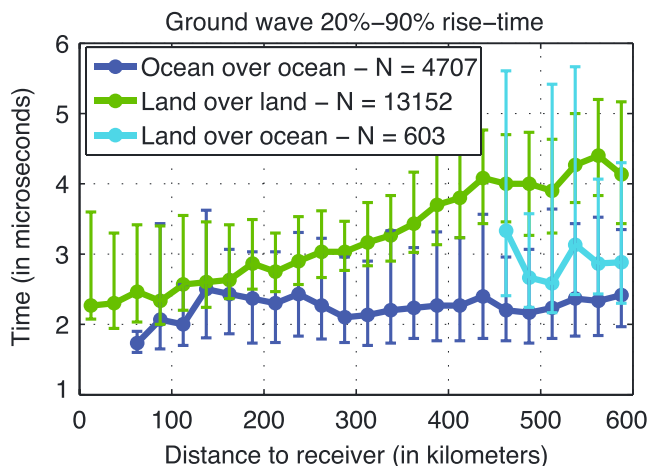


Figure 6. Measured 20%–90% waveform risetime, with the corresponding 25th and 75th percentile error bars, as a function of propagation distance to the receiver for three categories: (in blue) 4655 oceanic initial discharges with propagation path over the ocean, (in green) 12,716 land initial discharges with propagation path over land, and (in cyan) 603 land initial discharges with mixed propagation path.

components in the radiated fields and smoothen the shape of the rise of the waveform, leading to an increase in the measured ground wave risetime.

We compare oceanic to land lightning by analyzing the median waveform risetime at 500 km of the first category (ocean over ocean; in blue) to the risetime of the third category (land over mixed; in cyan). We measure the waveform risetime for oceanic (in blue) and land (in cyan) CGs to be 2.2 μs and 2.7 μs , respectively. As discussed earlier, longer risetimes in land CGs are in part due to the mixed propagation path (consisting of lower conductivity land), while ocean CGs only propagate over the ocean to the ship. Using the measured waveform risetimes and the simulation results at 500 km from Figure 4 (bottom), we can estimate an upper bound on the (potential) difference in oceanic and land channel-base current risetimes. We recall that, at 500 km, current risetimes of 3 μs and 4 μs lead to 20%–90% risetimes of 2.3 μs and 2.9 μs and to ground wave peaks of 23.6 nT and 22.3, respectively. These two simulation waveforms have similar 20%–90% risetimes as the medians of the first (2.2 μs) and third category (2.7 μs) of collected data. The source parameters corresponding to the simulations suggest that land and ocean initial –CGs have current risetimes within 1 μs (this difference represents our upper bound that assumes all of the increase is from a difference in current risetime and ignoring the partial propagation over land), resulting in <7% change in the LF peak. We note that this change cannot fully explain the higher GLD360 peak current estimates over the ocean, which are measured in VLF.

4.3. Return Stroke Speed

Figure 7 consists of three panels that use both the feature extraction and waveform aggregation tools to compare four groups of lightning strokes, all between 480 km and 520 km distance to the ship. The first group (in blue) consists of 1162 land initial –CGs which have GLD360-reported peak currents between 15 and 50 kA, the second (in red) consists of 23 land initial –CGs with peak currents higher than 100 kA, the third (in green) consists of 336 ocean initial –CGs with peak currents between 15 and 50 kA, and the fourth group (in black) consists of 61 ocean initial –CGs higher than 100 kA. The average waveforms of the four groups are displayed in Figure 7 (top), after normalizing the peaks to unity and setting them to time zero (as we are interested in the shape of the ground waves). Figure 7 (bottom row) shows the probability mass function of the waveform 20%–90% risetimes (bottom left) and 90%–20% falltimes (bottom right) of the four groups. Figure 7 (bottom row) also includes color-coded vertical lines which correspond to the medians of each distribution.

Figures 7 (top left) and 7 (bottom left) show that land waveforms (which propagate to the ship over land and ocean) tend to have longer risetimes and a smoother rising edge, in agreement with our results from section 4.2, due to the lower land conductivity. Figures 7 (top right) and 7 (bottom right) show that weak land (in blue) and weak ocean (in green) events have a similar falling edge and 90%–20% falltime distributions, which is also the case for strong land (in red) and strong ocean (in black) strokes. We like to note that we use the terms “weak” and “strong” to refer to low-peak-field and high-peak-field discharges. These results show that land and ocean events (of similar GLD360-reported intensity, discussed later) tend to have a similar ground wave fall shape, suggesting that other than the rising edge that is affected by ground conductivity, ocean and land ground waves have matching shapes. As shown in Figure 4 (bottom), different return stroke speeds lead to measurable changes in the shape of the ground wave, with faster return stroke speeds leading to a narrower pulse and a shorter 90%–20% waveform falltime. However, Figure 7 shows that land and oceanic waveforms have similar falltimes suggesting that it is unlikely for ocean and land discharges to have different return stroke speeds. In case the land and oceanic peak current difference was due to a difference in the return stroke speed, the waveform falltimes of oceanic waveforms should be shorter than land falltimes. In conclusion, our modeling and experimental analyses suggest that stronger oceanic lightning observations are unlikely to result from faster return stroke speed in oceanic CGs (due to a difference in the attachment process or the ground conductivity).

Interestingly, Figure 7 shows that weak ocean strokes (in green) have (on average) shorter risetimes and falltimes than strong ocean strokes (in black), and weak land strokes (in blue) have shorter risetimes and falltimes than strong land strokes (in red). This suggests that weaker GLD360-reported strokes, whether over land or over the ocean, tend to have (on average) narrower ground waves than stronger ones. The consistent difference in the shapes of weak and strong lightning CGs suggest that there could be a physical difference in the lightning source parameters of weak and strong discharges, such as the return stroke speed, although *Rakov* [1993] showed that experimental data do not support a relationship between the return stroke speed and peak current. These differences could have important practical applications to those interested in lightning physics, geolocation, and thunderstorm electrification.

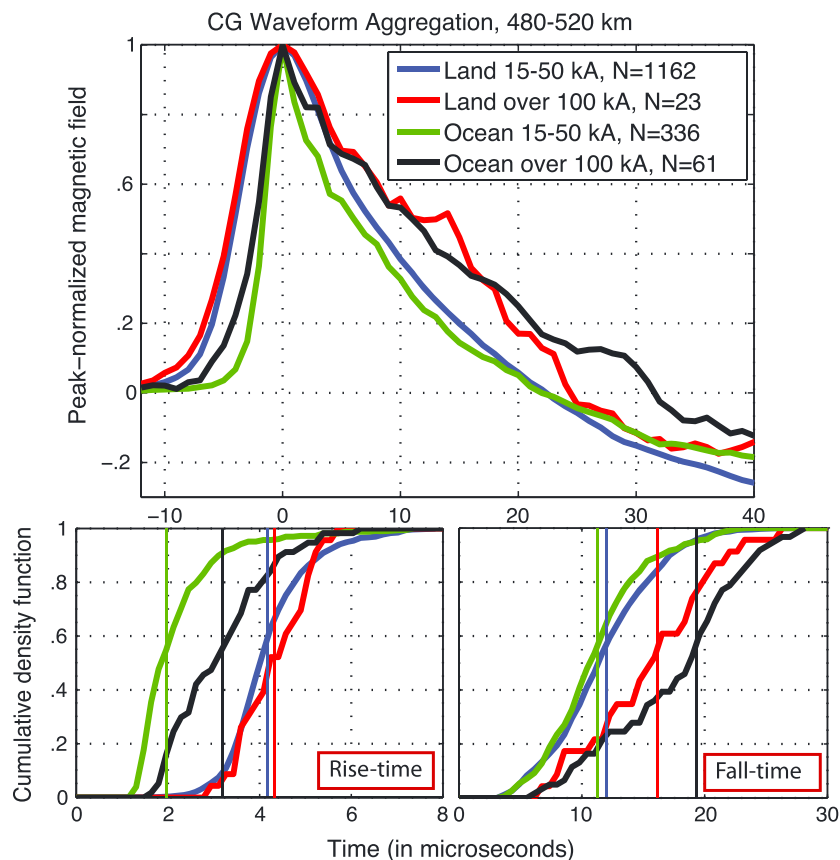


Figure 7. (top) Average peak-normalized waveform for four lightning groups between 480 km and 520 km distance to the ship: (in blue) 1162 land –CGs with GLD360 peak currents between 15 and 50 kA, (in red) 23 land –CGs >100 kA, (in green) 336 oceanic –CGs 15–50 kA, and (in black) 61 ocean –CGs >100 kA. (bottom row) Cumulative density function of the waveform (bottom left) 20%–90% risetimes and (bottom right) 90%–20% falltimes of the four groups, with vertical lines corresponding to the medians.

5. Summary

In this paper, we presented initial results from our shipborne experiment and introduced statistical tools to process the collected LF waveforms. We analyzed thousands of waveforms from land and oceanic discharges to study their risetime and falltime statistics. We constructed a computationally efficient electromagnetic model to simulate lightning ground waves, while accounting for Earth conductivity and curvature and compared simulation to experimental waveforms. We concluded that larger oceanic GLD360-reported peak radiated fields are unlikely to result from differences in oceanic and land channel-base current risetimes, current falltimes, or return stroke speeds. The higher radiated fields over the ocean seem to come from higher-amplitude return stroke currents, potentially due to meteorological differences between land and oceanic thunderstorms or due to differences in the lightning attachment process to ground or salt water.

Acknowledgments

This work is supported by the Defense Advanced Research Project Agency under grant HR0011-10-1-0058-P00001 to Stanford University with sub-contract to the Georgia Institute of Technology. GLD360 data are provided by Vaisala, Inc. Please contact fadiz@stanford.edu for more information about waveform data.

References

- Bardo, E. A., K. L. Cummins, and W. A. Brooks (2004), Lightning current parameters derived from lightning location systems, *International Conference on Lightning Detection*, Helsinki, Finland.
- Berger, K., R. Anderson, and H. Kroninger (1975), Parameters of lightning flashes, *Electra*, 80, 223–237.
- Budden, K. G. (1985), *The Propagation of Radio Waves: The Theory of Radio Waves of Low Power in the Ionosphere and Magnetosphere*, Cambridge Univ. Press, Cambridge, U. K.
- Christian, H. J., et al. (2003), Global frequency and distribution of lightning as observed from space by the Optical Transient Detector, *J. Geophys. Res.*, 108(D1), 4005, doi:10.1029/2002JD002347.
- Chronis, T. G. (2012), Preliminary lightning observations over Greece, *J. Geophys. Res.*, 117, D03113, doi:10.1029/2011JD017063.
- Cohen, M. B., U. S. Inan, and E. W. Paschal (2010), Sensitive broadband ELF/VLF radio reception with the AWESOME instrument, *IEEE Trans. Geosci. Remote Sens.*, 48, 3–17, doi:10.1109/TGRS.2009.2028334.
- Cohen, M. B., U. S. Inan, D. Piddiyachiy, N. G. Lehtinen, and M. Gokowski (2011), Magnetospheric injection of ELF/VLF waves with modulated or steered HF heating of the lower ionosphere, *J. Geophys. Res.*, 116, A06308, doi:10.1029/2010JA016194.

- Cohen, M. B., N. G. Lehtinen, and U. S. Inan (2012), Models of ionospheric VLF absorption of powerful ground based transmitters, *Geophys. Res. Lett.*, *39*, L24101, doi:10.1029/2012GL054437.
- Cooray, V. (1987), Effects of propagation on the return stroke radiation fields, *Radio Sci.*, *22*(5), 757–768.
- Cooray, V., and K. Cummins (2009), Propagation effects caused by multi-section mixed paths on electric fields of lightning return strokes, *X International Symposium on Lightning Protection*, Curitiba, Brazil.
- Cooray, V., and V. A. Rakov (2011), Engineering lightning return stroke models incorporating current reflection from ground and finitely conducting ground effects, *IEEE Trans. Electromagn. Compat.*, *53*(3), 773–781, doi:10.1109/TEM.2011.2113350.
- Cooray, V., M. Fernando, T. Sørensen, T. Götschl, and A. Pedersen (2000), Propagation of lightning generated transient electromagnetic fields over finitely conducting ground, *J. Atmos. Sol. Terr. Phys.*, *62*, 583–600, doi:10.1016/S1364-6826(00)00008-0.
- Cooray, V., R. Jayaratne, and K. L. Cummins (2014), On the peak amplitude of lightning return stroke currents striking the sea, *Atmos. Res.*, *149*, 372–376, doi:10.1016/j.atmosres.2013.07.012.
- Cummer, S. A., W. A. Lyons, and M. A. Stanley (2013), Three years of lightning impulse charge moment change measurements in the United States, *J. Geophys. Res. Atmos.*, *118*, 5176–5189, doi:10.1002/jgrd.50442.
- Cummins, K. L., and M. J. Murphy (2009), An overview of lightning locating systems: History, techniques, and data uses, with an in-depth look at the U. S. NLDN, *IEEE Trans. Electromagn. Compat.*, *51*(3), 499–518.
- Cummins, K. L., M. J. Murphy, E. A. Bardo, W. L. Hiscox, R. B. Pyle, and A. E. Pifer (1998), A combined TOA/MDF technology upgrade of the U.S. National Lightning Detection Network, *J. Geophys. Res.*, *103*, 9035–9044.
- Cummins, K. L., J. A. Cramer, W. A. Brooks, and E. P. Krider (2005), On the effect of land:sea and other earth surface discontinuities on LLS-inferred lightning parameters, *VIII International Symposium on Lightning Protection*, São Paulo, Brazil.
- Fullekrug, M., C. Price, Y. Yair, and E. R. Williams (2002), Letter to the editor intense oceanic lightning, *Ann. Geophys.*, *20*(1), 133–137.
- Graf, K. L., N. G. Lehtinen, M. Spasojevic, M. B. Cohen, R. A. Marshall, and U. S. Inan (2013), Analysis of experimentally validated trans-ionospheric attenuation estimates of VLF signals, *J. Geophys. Res. Space Physics*, *118*, 2708–2720, doi:10.1002/jgra.50228.
- Hutchins, M. L., R. H. Holzworth, K. S. Virts, J. M. Wallace, and S. Heckman (2013), Radiated VLF energy differences of land and oceanic lightning, *Geophys. Res. Lett.*, *40*, 2390–2394, doi:10.1002/grl.50406.
- Lehtinen, N. G., and U. S. Inan (2008), Radiation of ELF/VLF waves by harmonically varying currents into a stratified ionosphere with application to radiation by a modulated electrojet, *J. Geophys. Res.*, *113*, A06301, doi:10.1029/2007JA012911.
- Lehtinen, N. G., and U. S. Inan (2009), Full-wave modeling of transionospheric propagation of VLF waves, *Geophys. Res. Lett.*, *36*, L03104, doi:10.1029/2008GL036535.
- Lehtinen, N. G., T. F. Bell, L. Qiu, M. B. Cohen, and U. S. Inan (2012), Full wave modeling of VLF wave scattering and propagation in curvilinear stratified ionosphere, in *2012 International Conference on Electromagnetics in Advanced Applications (ICEAA)*, pp. 195–198, IEEE, Cape Town, South Africa, doi:10.1109/ICEAA.2012.6328619.
- Lyons, W. A., M. Uliasz, and T. E. Nelson (1998), Large peak current cloud-to-ground lightning flashes during the summer months in the contiguous United States, *Mon. Weather Rev.*, *126*, 2217–2233, doi:10.1175/1520-0493(1998)126<2217:LPCTG>2.0.CO;2.
- MacGorman, D. R., and C. D. Morgenstern (1998), Some characteristics of cloud-to-ground lightning in mesoscale convective systems, *J. Geophys. Res.*, *103*, 14,011–14,023.
- Mallick, S., et al. (2014a), Performance characteristics of the NLDN for return strokes and pulses superimposed on steady currents, based on rocket-triggered lightning data acquired in Florida in 2004–2012, *J. Geophys. Res. Atmos.*, *119*, 3825–3856, doi:10.1002/2013JD021401.
- Mallick, S., et al. (2014b), Lightning return stroke speed, *J. Lightning Res.*, *41*(10), 3636–3642, doi:10.1002/2014GL059920.
- Marshall, R. A. (2012), An improved model of the lightning electromagnetic field interaction with the d-region ionosphere, *J. Geophys. Res.*, *117*, A03316, doi:10.1029/2011JA017408.
- Nag, A., V. A. Rakov, and K. L. Cummins (2014), Positive lightning peak currents reported by the U.S. National Lightning Detection Network, in *IEEE TEMC*, IEEE, doi:10.1109/TEM.2013.2280000.
- Nag, A., et al. (2011), Evaluation of U. S. National Lightning Detection Network performance characteristics using rocket-triggered lightning data acquired in 2004–2009, *J. Geophys. Res.*, *116*, D02123, doi:10.1029/2010JD014929.
- Norton, K. A. (1936), The propagation of radio waves over the surface of the Earth and in the upper atmosphere, *Proc. Inst. Radio Eng.*, *24*(10), 1367–1387.
- Nucci, C. A., C. Mazzetti, F. Rachidi, and M. Ianoz (1988), On lightning return stroke models for the lemp calculations, *Proceedings of 19th International Conference on Lightning Protection*, Graz, pp. 463–469.
- Orville, R. E., and G. R. Huffines (2001), Cloud-to-ground lightning in the United States: NLDN results in the first decade 1989–98, *Mon. Weather Rev.*, *129*, 1179–1193.
- Orville, R. E., G. R. Huffines, W. R. Burrows, R. L. Holle, and K. L. Cummins (2011), The North American Lightning Detection Network (NALDN) analysis of flash data: 2001–09, *Mon. Weather Rev.*, *139*, 1305–1322, doi:10.1175/2010MWR3452.1.
- Rakov, V. (1993), Lightning return stroke speed, *J. Lightning Res.*, *1*(1935), 80–89.
- Rakov, V. A., and A. A. Dulzon (1987), Calculated electromagnetic fields of lightning return stroke, *Tekh. Elektrodinam.*, *1*, 87–89.
- Rakov, V. A., and M. A. Uman (2007), *Lightning: Physics and Effects*, Cambridge Univ. Press, Cambridge, U. K.
- Said, R. K., U. S. Inan, and K. L. Cummins (2010), Long-range lightning geo-location using a VLF radio atmospheric waveform bank, *J. Geophys. Res.*, *115*, D23108, doi:10.1029/2010JD013863.
- Said, R. K., M. B. Cohen, and U. S. Inan (2013), Highly intense lightning over the oceans: Estimated peak currents from global GLD360 observations, *J. Geophys. Res. Atmos.*, *118*, 6905–6915, doi:10.1002/jgrd.50508.
- Thottappillil, R., and A. Uman (1993), Comparison of lightning return-stroke models, *J. Geophys. Res.*, *98*, 22,903–22,914.
- Turman, B. N. (1977), Detection of lightning superbolts, *J. Geophys. Res.*, *82*(18), 2566–2568, doi:10.1029/JC082i018p02566.
- Tyahla, L. J., and R. E. Lopez (1994), Effect of surface conductivity on the peak magnetic field radiated by first return strokes in cloud-to-ground lightning, *J. Geophys. Res.*, *99*, 10,517–10,525.
- Williams, E., V. Mushtak, D. Rosenfeld, S. Goodman, and D. Boccippio (2005), Thermodynamic conditions favorable to superlative thunderstorm updraft, mixed phase microphysics and lightning flash rate, *Atmos. Res.*, *76*, 288–306, doi:10.1016/j.atmosres.2004.11.009.
- Zoghoghzy, F. G., M. B. Cohen, R. K. Said, and U. S. Inan (2013), Statistical patterns in the location of natural lightning, *J. Geophys. Res. Atmos.*, *118*, 787–796, doi:10.1002/jgrd.50107.